Analysis of centrifugal convection in rotating pipes

Vladimir Shtern,[a] Valery Zimin, and Fazle Hussain
University of Houston, Houston, Texas 77204-4006

(Received 20 December 2000; accepted 30 April 2001)

New exact solutions, obtained for centrifugal convection of a compressible fluid in pipes and annular pipes, explain axially elongated counterflow and energy separation—poorly understood phenomena occurring in vortex devices, e.g., hydrocyclones and Ranque tubes. Centrifugal acceleration (which can be up to 10^6 times gravity in practical vortex tubes), combined with an axial gradient of temperature (even small), induces an intense flow from the cold end to the hot end along the pipe wall and a backflow near the axis. To account for large density variations in vortex devices, we use the axial temperature gradient as a small parameter instead of the Boussinesq approximation. For weak pipe rotation, the swirl is of solid-body type and solutions are compact: $v_z/v_{za}=1-4y^2+3y^4$ and $(T-T_w)/(T_a-T_w)=(1-y^2)^3$; where $y=r/r_w$, the subscripts w and a denote values of axial velocity v_z, temperature T, and radial distance r, at the wall and on the axis. The axial gradient of pressure, being proportional to $3y^2-1$, has opposite directions near the wall, $y=1$, and near the axis, $y=0$; this explains the counterflow. With increasing pipe rotation, the flow starts to converge to the axis. This causes important new effects: (i) the density and swirl velocity maxima occur away from the wall (vortex core formation), (ii) the temperature near the axis becomes lower than near the wall (the Ranque effect), (iii) the axial gradient of temperature drops from the wall to the axis, and (iv) the total axial heat flux (Nu) reaches its maximum $\mathrm{Nu}_{\max}\approx 4000$ and then decreases as swirl increases. These features can be exploited for the development of a micro-heat-exchanger, e.g., for cooling computer chips.
[DOI: 10.1063/1.1384890]

I. INTRODUCTION

We study the flow of a compressible fluid in rotating pipes in the hope of developing innovative heat exchangers. Radial acceleration due to rotation and an axial temperature gradient induce an axially elongated circulatory flow. Fluid moves along the temperature gradient near the wall and back near the axis of a pipe (or near the inner wall of an annulus, Fig. 1). Therefore, such a counterflow transports the cooled fluid (from the cold end) along the wall and transports the heated fluid (from the hot end) along the axis. This centrifugal convection can provide efficient heat transfer between the hot and cold ends and, in addition, can protect the pipe sidewall against overheating.

To understand the flow direction, consider the pressure distribution induced by the combined effect of centrifugal force and heating. The centrifugal force causes a radial increase in pressure, and the imposed axial gradient of temperature makes this increase z dependent. That is, due to the density difference between the cold and hot ends, the radial increase in pressure near the cold end, $p_{wc}-p_{ac}$, is larger than the increase, $p_{wh}-p_{ah}$, near the hot end (Figs. 1 and 11). Therefore, there is an axial gradient of pressure, which is parallel to the temperature gradient near the axis ($p_{ah}>p_{ac}$) and antiparallel along the outer wall ($p_{wc}>p_{wh}$). Driven by such a pressure distribution, the counterflow can have a large axial extent. For example, counterflow exists over a hundred diameters in vortex tubes. The counterflow occurs despite turbulent mixing at Reynolds numbers exceeding 10^5 in these devices! This counterflow can significantly enhance heat transfer between the hot and cold ends—an effect important for heat exchangers.

While similar counterflows emerge in thermogravitational convection as well, centrifugal acceleration can intensify fluid motion. This swirling flow can be stable for rather large Reynolds numbers due to (i) the Taylor–Proudman constraint, and (ii) centrifugal density stratification. These two features—flow intensification and stabilization—are favorable for the development of efficient heat exchangers.

Thermal convection in rotating systems has been extensively studied for astrophysical and geophysical applications, e.g., for large-scale circulation in the Earth's atmosphere caused by the temperature difference between equatorial and polar regions. Barcilon and Pedlosky[1] and Homsy and Hudson[2] investigated centrifugally generated convection in a rapidly rotating cylinder using the boundary-layer approximation for $\underline{l}\leqslant O(1)$; $\underline{l}\equiv l/r_w$, where $2l$ and r_w are the cylinder height and radius. Hart[3] (2000) reviewed and studied in detail the case $\underline{l}\ll 1$, which is relevant for the Earth's polar regions. Busse[4] and co-workers (see Ref. 5 for a review) considered convection in a rotating cylindrical annulus subjected to a *radial* temperature gradient, a case relevant to the equatorial regions. For planets and stars, the centrifugal to gravity acceleration ratio, g_c/g, is small, whereas in vortex tubes, g_c/g is very large (e.g., 10^6), as is l. Here, we consider small *axial* temperature gradients and large g_c/g and l

[a]Electronic mail: mece21w@jetson.uh.edu

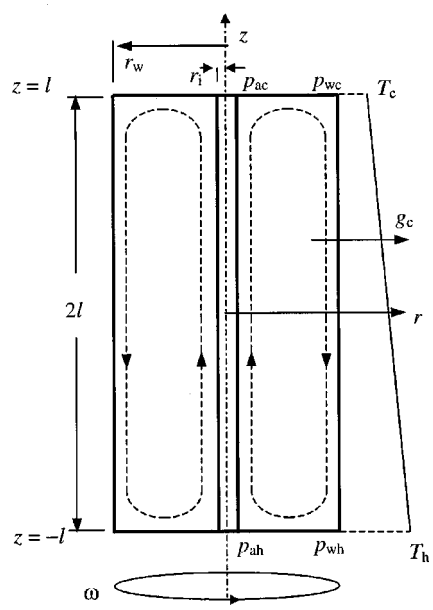

FIG. 1. Schematic of a centrifugal heat exchanger. An annular container filled with a gas rotates around its axis with angular velocity ω. The axial gradient of temperature and centrifugal acceleration g_c induce thermal convection (dashed curves) which intensifies the heat transfer between the hot ($z=-l$) and cold ($z=l$) ends.

for the idealized problem of convection in rotating pipes.

For generality and comparison with known results, we also consider annular pipes. The problem of centrifugal convection in a narrow-gap annulus is closely related to the problem of thermogravitational convection in a horizontal layer subjected to a horizontal temperature gradient. Birikh[6] obtained an analytical solution for this planar counterflow, which agrees well with experiment.[7] It is interesting that the experiment[7] reveals no instability even for Rayleigh numbers $\mathrm{Ra}>10^4$, although theory[8] predicts that the Birikh flow becomes unstable to longitudinal-vortex disturbances for $\mathrm{Ra}>10^3$.

While buoyancy flows typically remain laminar for $\mathrm{Ra}<10^4$, heat transfer due to convection is a few orders of magnitude greater than that due to conduction at $\mathrm{Ra}=10^4$. As g_c becomes large, even a small temperature difference leads to intense heat transfer by centrifugal convection. We estimate that $g_c/g \geqslant 10^4$ in centrifugal heat exchangers and therefore neglect gravity in this paper. This large acceleration makes the flow very intense even for a small axial temperature gradient (typical for devices with large length/radius ratios). This justifies our approach, where the dimensionless axial gradient of temperature serves as a small parameter.

Since the Boussinesq approximation is not valid for large density variations (typical of vortex tubes), we use a different approach: power expansion with respect to $\epsilon \equiv \underline{l}^{-1}\Delta T/T_R$. Here $2\Delta T \equiv T_h - T_c$ (Fig. 1) is the temperature difference between the hot and cold ends, and $T_R \equiv (T_h + T_c)/2$ is the reference temperature. For large aspect ratio $\underline{l}$, ϵ is small even when $\Delta T/T_R$ is of $O(1)$.

In addition to ϵ, another important control parameter is the swirl Reynolds number $\mathrm{Re}_s = \omega r_w^2/\nu$; where ω is the angular velocity of the outer wall (Fig. 1) and ν is the kinematic viscosity. These parameters, ϵ and Re_s, characterize the axial temperature gradient and rotation—two factors that together drive the centrifugal convection. As we will show, the axial velocity is proportional to $\epsilon\,\mathrm{Re}_s$, the induced radial temperature gradient is proportional to $\epsilon^2\,\mathrm{Re}_s^2$, and the radial velocity is proportional to $\epsilon^2\,\mathrm{Re}_s$ (important nonparallel effect for rapid rotation).

First, we consider ϵ so small that $\epsilon\,\mathrm{Re}_s \ll 1$ even at large Re_s. In this case, the equation for the axial velocity becomes linear and decoupled from the equation for the radial distribution of temperature. This allows us to obtain solutions in polynomial forms. In the limiting case of the gap between cylinders tending to zero, our analytical solutions coincide with those for the horizontal layer subjected to a horizontal temperature gradient in the gravity field, obtained by Birikh[6] and by Kirdyashkin[7] under the Boussinesq approximation. This agreement shows, in particular, that our approach is quite consistent with the Boussinesq approximation for small $\epsilon\,\mathrm{Re}_s$.

Next, we consider moderate rotation, where $\epsilon \ll 1$ but $\epsilon\,\mathrm{Re}_s$ is of $O(1)$. In this case, the radial variations of temperature contribute to the pressure distribution; therefore, the Boussinesq approximation is not applicable. The equations for velocity and temperature become coupled and nonlinear; therefore, in this case, we obtain solutions numerically.

Finally, we consider rapid rotation, $\epsilon\,\mathrm{Re}_s \gg 1$, where a weak, $O(\epsilon)$, deviation from parallel flow occurs, which is also a non-Boussinesq effect. The flow converges to the axis causing that (i) the density reaches its maximum away from the wall; (ii) in addition to the core with solid-body rotation, an outer region appears where swirl is nearly potential; and (iii) the axial gradient of temperature drops from the wall to the axis.

Thus, new features of our problem are: (a) intense axial counterflow due to large g_c/g, (ii) high density gradients due to swirl, and (iii) flow convergence to the axis. These are essential features for centrifugal heat exchangers.

In the remainder of the paper we introduce the governing equations (Sec. II), obtain solutions for weak rotation (Sec. III), consider effects of end walls (Sec. IV), rapid rotation (Sec. V), and the radial velocity (Sec. VI), and discuss the results (Sec. VII).

II. REDUCTION OF THE GOVERNING EQUATIONS

We start with the equations governing steady flows of a viscous compressible fluid,

$$\nabla\cdot(\rho\mathbf{v})=0, \quad \rho(\mathbf{v}\cdot\nabla)\mathbf{v}=\mu\Delta\mathbf{v}-\nabla p+(\mu/3)\nabla(\nabla\mathbf{v}),$$
$$\rho c_p(\mathbf{v}\cdot\nabla)T=\kappa\Delta T+(\mathbf{v}\cdot\nabla)p, \quad p=\rho RT. \tag{1}$$

Here $\mathbf{v}$ is the velocity vector; ρ, p, and T are density, pressure, and temperature; μ and κ are viscosity and thermal conductivity; c_p is the specific heat at constant pressure; and R is the gas constant. The contribution of viscous dissipation in the energy equation is neglected.

We use cylindrical coordinates $\{r,\phi,z\}$ and consider flow between two coaxial cylinders under the following conditions: (i) the flow is axisymmetric, $\partial/\partial\phi=0$, (ii) μ and κ

are constant, and (iii) the radial velocity is zero, $v_r=0$ (this condition will be omitted in Secs. IV and VI). Then Eq. (1) reduces to

$$\partial(\rho v_z)/\partial z=0, \tag{2a}$$

$$\rho v_\phi^2/r=\partial(p-2/3\mu\partial v_z)\partial r, \tag{2b}$$

$$\rho v_z\partial v_\phi/\partial z=\mu(\partial^2 v_\phi/\partial r^2+r^{-1}\partial v_\phi/\partial r-v_\phi/r^2+\partial^2 v_\phi/\partial z^2), \tag{2c}$$

$$\rho v_z\partial v_z/\partial z=-\partial/\partial z(p-2/3\mu\partial v_z/\partial z)+\mu(\partial^2 v_z/\partial r^2+r^{-1}\partial v_z/\partial r+\partial^2 v_z/\partial z^2), \tag{2d}$$

$$\rho v_z c_p\partial T/\partial z=v_z\partial p/\partial z-2/3\mu(\partial v_z/\partial z)^2+\kappa(\partial^2 T/\partial r^2+r^{-1}\partial T/\partial r+\partial^2 T/\partial z^2), \tag{2e}$$

$$p=\rho RT. \tag{2f}$$

We will study those solutions of (2) which model flows in centrifugal heat exchangers and start with the case of small temperature gradients (Sec. III).

III. CENTRIFUGAL CONVECTION

A. Axial flow at small temperature gradients and weak swirl

1. Isothermal density stratification caused by rotation

First, consider a z-independent solution for a swirling flow with $v_z=0$ in the gap, $r_i\leqslant r\leqslant r_w$, between two cylinders. In this case, Eq. (2c) yields a solution for swirl that is a superposition of solid-body and potential-vortex flows,

$$v_\phi=\omega r+\Gamma/r, \tag{3}$$

where ω and Γ are integration constants which are specified by the imposed rotational velocities of the cylinders.

The general solution of (2e) is $T=T_R+C\ln r$, where T_R (reference temperature) and C are constant. Here we put $C=0$, i.e., we consider the temperature at the cylinder walls to be equal. Then, (2f) yields

$$p_0(r)=RT_R\rho_0(r), \tag{4a}$$

where the subscript "0" denotes the leading term in a small-parameter expansion (see the following).

Upon substituting (3) and (4a) in (2b) and integrating we get

$$\rho_0(r)=\rho_{0i}\exp[I(r)], \tag{4b}$$

where ρ_{0i} is the density at the inner cylinder, and the integral

$$I(r)=\int v_\phi^2/(RT_R r)dr \tag{4c}$$

runs from r_i to r. Solution (4b) gives density stratification due to swirl used below.

2. Counterflow induced by axial gradient of temperature

Next, we impose the following axial temperature gradient at the walls:

$$T=T_R(1-\epsilon z/r_w). \tag{5}$$

When $v_z=0$, (2e) implies that (5) is valid for all r as well. For a cylindrical container (Fig. 1), $\epsilon=\frac{1}{2}(r_w/l)(T_h-T_c)/T_R$ and $T_R=(T_h+T_c)/2$. A clear limitation for (5) is that $\epsilon z/r_w$ must be smaller than 1, so that $\epsilon<r_w/l$. When $r_w/l\ll 1$, ϵ is small even for $\frac{1}{2}(T_h-T_c)/T_R$ close to 1. Therefore, we can use ϵ as a small parameter in the following expansion.

The axial temperature gradient induces an axial flow in a rotating pipe. This occurs because the radial difference in pressure, p_w-p_a, is smaller near the hot end (where fluid has small density) than near the cold end (where fluid has large density); here, the subscripts w and a denote values at the wall and at the axis. Accordingly, $p_{wc}>p_{wh}$ and $p_{ac}<p_{ah}$; here, the subscripts c and h denote the cold and hot ends (Fig. 1). These opposite axial gradients of pressure drive a flow from the cold end to the hot end along the wall and a reversed flow near the axis.

Deducing the governing equation for axial flow from (2), we first note that (2a) implies that the product ρv_z depends only on r. Using the expansion,

$$\rho=\rho_0(r)+O(\epsilon),\quad v_z=\epsilon v_{z1}+O(\epsilon^2),$$

we see that v_{z1} also depends only on r. Then (2d) yields for the $O(\epsilon)$ terms,

$$\partial p/\partial z=\epsilon\mu(d^2 v_{z1}/dr^2+r^{-1}dv_{z1}/dr), \tag{6}$$

i.e., p has a contribution which is a linear function of z:

$$p=p_0(r)-\epsilon z/r_w p_1(r)+O(\epsilon^2). \tag{7}$$

Now using (2f), (4a), (5), and (7) we get

$$\rho=\rho_0(r)+\epsilon z/r_w\rho_1(r)+O(\epsilon^2) \tag{8}$$

and

$$p_1(r)=RT_R[\rho_0(r)-\rho_1(r)]. \tag{9}$$

Since $\partial v_z/\partial z$ is of $O(\epsilon^2)$, we find from the $O(\epsilon)$ terms in (2b) that

$$d\rho_1/dr-\rho_1 v_\phi^2/(RT_R r)=d\rho_0/dr.$$

Substituting (4b) and integrating we get

$$\rho_1=(\rho_{1i}+\rho_{0i}I)\exp I, \tag{10}$$

whence, with the help of (9), we obtain

$$p_1=RT_R(\rho_{0i}-\rho_{1i}-\rho_{0i}I)\exp I. \tag{11}$$

Here ρ_{1i} is a constant of integration to be determined.

Finally, use of (7) and (11) transforms (6) into the following form:

$$d^2 v_{z1}/dr^2+r^{-1}dv_{z1}/dr=(I-c)\exp I\,\rho_{0i}RT_R/(\mu r_w), \tag{12}$$

where $c=1-\rho_{1i}/\rho_{0i}$.

The no-slip conditions at the cylinder walls,

$$v_{z1}(r_w)=0, \tag{13}$$

$$v_{z1}(r_i)=0, \tag{14}$$

make the problem (12)–(14a) mathematically closed. There is also the additional integral condition that the mass flow rate through any cross section, $z=\text{const}$, is zero,

$$\int \rho_0(r)v_{z1}(r)r\,dr=0, \tag{15}$$

where the integration runs from r_i to r_w. This condition determines the parameter c.

In the case of a (nonannular) pipe, where $r_i=0$, the axisymmetry condition,

$$dv_{z1}/dr(0)=0, \tag{14$'$}$$

replaces (14).

A dimensionless form of (12) is

$$(yW')'=y(I-c)\exp I. \tag{16}$$

Here $W=v_{z1}(\rho_{0i}RT_Rr_w/\mu)^{-1}$,

$$I=\int_a^y b(v^2/y)dy, \tag{17}$$

$a=r_i/r_w$, $b=\omega^2r_w^2/(RT_R)$, $v=v_\phi/(\omega r_w)$, and the prime denotes differentiation with respect to $y=r/r_w$. Since γRT_R is the squared sonic velocity (γ being the specific heat ratio) and ωr_w is the maximum rotation velocity, parameter b is a modified Mach number for the swirl.

Now we consider a few particular cases where (16) has analytical solutions. We start with the narrow-gap case, where it is possible to compare the results with those for the planar flow.[6]

B. Narrow-gap flow

Consider the limiting case where (i) both cylinders rotate with the same angular velocity (i.e., $\Gamma=0$), and (ii) the gap between the cylinders is small compared with the radius of the outer cylinder, $2\delta\equiv r_w-r_i\ll r_w$. Then, v and y are both very close to 1, so that we can substitute $v^2/y=1$ in (17) as $\delta/r_w\to 0$; this substitution yields $I=b(y-a)$.

It is convenient to introduce a scaled coordinate x which is $O(1)$ in the gap:

$$x=(y-a)/\Delta-1,\quad \Delta=(1-a)/2=\delta/r_w.$$

Since $I=b(1+x)\Delta$ tends to zero as $a\to 1$, we take $\exp I=1$. In this case, (16) reduces to

$$d^2W/dx^2=[b(1+x)\Delta-c]^2.$$

Integrating under conditions (13) and (14) and choosing $c=b\Delta$, we find that

$$W=(x^3-x)b\Delta^3/6. \tag{18a}$$

For comparison with the planar flow, we introduce the Reynolds number, $\mathrm{Re}=\rho_{0i}v_{zm}\delta/\mu$, and the Grashof number, $\mathrm{Gr}=\epsilon g_c\delta^4\rho_{0i}^2/(\mu^2r_w)$, where v_{zm} is the maximal axial velocity, the length scale $\delta=(r_w-r_i)/2$, and $g_c=\omega^2r_w$ is the maximum centrifugal acceleration. Then (18a) yields

$$\mathrm{Re}=\mathrm{Gr}/\sqrt{243}. \tag{18b}$$

Formulas (18a) and (18b) coincide with those found by Birikh[6] for a fluid flow between horizontal plates induced by a horizontal gradient of temperature and subjected to only gravity (i.e., no centrifugal effect). This coincidence is not surprising because (i) centrifugal acceleration is nearly uniform (as is the gravitational acceleration in the Birikh problem), (ii) density is also nearly uniform, and (iii) the cylinder curvature is negligible when the gap between cylinders is small compared with the cylinder radius. However, an important difference is that the same temperature gradient induces significantly stronger (by a factor of g_c/g) flow in our case (e.g., at $\omega r_w=100$ m/s and $r_w=0.1$ m, $g_c/g=10^4$).

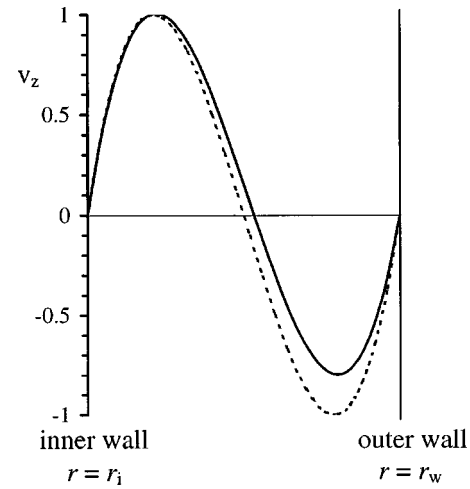

FIG. 2. The axial counterflow induced by the axial temperature gradient in a rotating annular pipe for $r_i/r_w=0.5$ (solid curve) and $r_i/r_w\to 1$ (broken curve).

C. Finite-gap flow at weak swirl

Analytical solutions in terms of elementary functions also exist for any values of r_i and r_w when $b\ll 1$. In this case, replacing $\exp I$ by 1 in (16) and integrating we get

$$W=[(y^4-1)/32+\tfrac{1}{2}\Gamma^*y^2\ln y-\tfrac{1}{4}\Gamma^{*2}\ln^2 y]+C_0(1-y^2)+C_1\ln y, \tag{18c}$$

where

$$C_1=[(1-a^4)/(32\ln a)+\tfrac{1}{2}\Gamma^*a^2-\tfrac{1}{4}\Gamma^{*2}\ln a-C_0(1-a^2)/\ln a],$$

$$C_0=[24\Gamma^*(a^2\Gamma^*+\Gamma^*-2a^2)\ln^2 a+4(1-a^2)(1+a^2+a^4+3\Gamma^*+6\Gamma^{*2}-9a^2\gamma)\ln a-3(1-a^2)^2(1+a^2)]/[96(1-a^2)/(1-a^2+\ln a+a^2\ln a)],$$

and $\Gamma^*=\Gamma/(\omega r_w^2)$. Figure 2 depicts the profiles of v_z (normalized by its maximum value) according to (18a) and (18b) at $\Gamma^*=0$. In the finite-gap annulus ($a\equiv r_i/r_w=0.5$, solid curve), the radial extent of the descending flow and its maximum velocity are reduced in comparison with those for the narrow gap ($a\to 1$, broken curve).

D. Flow in a pipe

As another example, consider the flow in a rotating pipe, i.e., $r_i=0$, $\Gamma=0$, and $v=y$. Now, $I=by^2/2$, and integration of (16) yields

$$W'=[1-\exp(by^2/2)](1-c)/(by)+\tfrac{1}{2}y\exp(by^2/2). \tag{19a}$$

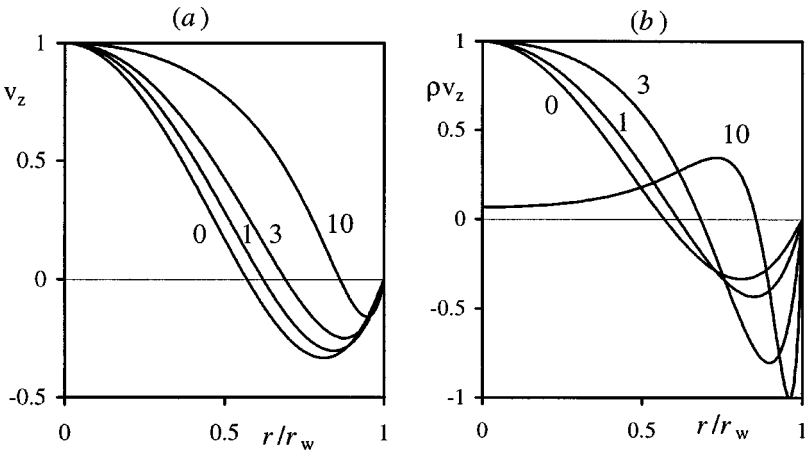

FIG. 3. The radial distribution of axial velocity v_z and mass flow ρv_z (normalized by their maximum values) at different swirl, characterized by $b=\omega^2 r_w^2/(RT_R)$ shown near the curves.

One more integration yields

$$W=\{\exp(by^2/2)-\exp(b/2)+(1+c)[2\ln y+\mathrm{Ei}(b/2)-\mathrm{Ei}(by^2/2)]\}/(2b). \tag{19b}$$

Here Ei is the exponential integral function, $\mathrm{Ei}(z)=-\int_{-z}^{\infty}\exp(-t)t^{-1}\,dt$. Since for small z, $\mathrm{Ei}(z)=\ln z+\mathrm{EC}+z+O(z^2)$, where EC ($\approx$0.577 216) is the Euler constant,

$$W(0)=\{1-\exp(b/2)+(1+c)\times[\mathrm{Ei}(b/2)-\ln(b/2)-\mathrm{EC}]\}/(2b). \tag{19c}$$

Finally, from (15) it follows that

$$c=\tfrac{1}{2}[\exp(b/2)-1]^2/[\mathrm{Ei}(b)-2\,\mathrm{Ei}(b/2)+\ln(b/4)+\mathrm{EC}]-1. \tag{19d}$$

For $b<1$, replacing $\exp(by^2/2)$ by $1+by^2/2$ in (19a) and integrating we obtain the following polynomial approximation:

$$W=(1-y^2)c/4-(1-y^4)b(1-c)/32-(1-y^6)b^2/144, \tag{19e}$$

where $c=b(1+35b/80+b^2/20)/(6+2b+3b^2/16)$.

Normalizing W by its maximum value $W(0)$,

$$w(y)=W(y)/W(0),$$

we find that in the limiting case of $b\to 0$, w has a compact polynomial form,

$$w=1-4y^2+3y^4. \tag{20a}$$

The maximum downward velocity $w_{\min}=-1/3$ is located at $y_{\min}=(2/3)^{1/2}=0.8165$, and the boundary between the counterflows (where $w=0$) is $y_s=1/\sqrt{3}=0.577$.

For $b\ll 1$, $W(0)=b/96$, so that the dimensional axial velocity is

$$v_z=\omega r_w w(y)\epsilon\,\mathrm{Re}_s/96, \tag{20b}$$

where $\mathrm{Re}_s=\rho_{0i}\omega r_w^2/\mu$ is the swirl Reynolds number. Now we recall that ϵ is the dimensionless temperature gradient, $\epsilon=r_w T_R^{-1}\partial T/\partial z$, and introduce the Grashof number $\mathrm{Gr}=\epsilon g_c r_w^3\rho_{0i}^2/\mu^2$, where $g_c=\omega^2 r_w$ is the maximal centrifugal acceleration (note that $\mathrm{Gr}=\epsilon\,\mathrm{Re}_s^2$). Then from (20b) at $y=0$, we get

$$\mathrm{Re}=\mathrm{Gr}/96,$$

where $\mathrm{Re}=\rho_{0i}v_{za}r_w/\mu$ is the Reynolds number based on the velocity on the axis, v_{za}.

Figure 3(a) depicts the $w(y)$ profiles at different values of swirl b. In addition to the above-mentioned analytical solutions [e.g., curve 0 corresponds to (20a)], we have solved the problem numerically [numerical integration appears more convenient than the use of Ei in (19b)–(19d)]. For $b\leqslant 1$, the analytical, (19e) and (20a), and numerical results coincide within the accuracy of drawing in Fig. 3. For $b>1$, Fig. 3 shows the numerical results. High-speed rotation ($b\gg 1$) compresses the region of descending flow to the sidewall and decreases the maximum downward velocity because density near the wall becomes significantly larger than near the axis [Fig. 3(b) shows the ρv_z profiles for the same b].

E. Radial distribution of temperature

In (2e), the left-hand side and the first term on the right-hand side are of $O(\epsilon^2)$, while the second term on the right-hand side is of $O(\epsilon^4)$ and therefore can be neglected. Note that the $O(\epsilon^2)$ terms are z independent. So we can introduce $\vartheta(y)$ through the following expansion:

$$T=T_R[1-\epsilon z/r_w+\epsilon^2\vartheta(y)+O(\epsilon^3)]. \tag{21}$$

The equation for the dimensionless temperature perturbation, $\vartheta(y)$, which follows from (2e), (6), and (16), is

$$(y\vartheta')'=-\mathrm{Pr}\,\mathrm{Re}_s^2\,b^{-1}y\exp I[1+(I-c)(1-1/\gamma)]W, \tag{22}$$

where $\mathrm{Pr}=c_p\mu/\kappa$, $\gamma=c_p/c_v$, and c_v is the specific heat at constant volume.

Boundary conditions for an annulus with fixed temperatures at the walls are

$$\vartheta(a)=0,\quad \vartheta(1)=0, \tag{23a}$$

and for a pipe are

$$\vartheta'(0)=0,\quad \vartheta(1)=0. \tag{23b}$$

Since integrating the right-hand side of (22) over the interval $0\leqslant y\leqslant 1$ yields a nonzero quantity in general, we

cannot apply the adiabatic-wall condition, $\vartheta'(1)=0$. One exception is the case $\gamma=1$, when (15) allows adiabatic walls.

The second exception is the narrow-gap case, $\Delta=\delta/r_w \ll 1$. As $\Delta\to 0$, the term involving γ in (22) vanishes (both I and c are proportional to Δ), and (22) reduces to

$$\vartheta''=-\Delta^2 \operatorname{Pr} \operatorname{Re}_s^2 b^{-1} W, \tag{24a}$$

where the prime denotes differentiation with respect to $x=(y-a)/\Delta-1$. Using (18a) we transform (24a) into

$$\vartheta''=\Delta^5 \operatorname{Pr} \operatorname{Re}_s^2 (x-x^3)/6. \tag{24b}$$

Since integrating the right-hand side of (24b) over the interval $-1\leqslant x\leqslant 1$ yields zero, both the fixed-temperature and the adiabatic conditions can be applied at the walls. For the fixed-temperature condition, $\vartheta(-1)=\vartheta(1)=0$, the solution of (24b),

$$\vartheta=\Delta^5 \operatorname{Pr} \operatorname{Re}_s^2 (10x^3-3x^5-7x)/360, \tag{24c}$$

coincides (after replacement of g by $g_c=\omega^2 r_w$) with that found by Birikh.[6] For the condition $\vartheta'(-1)=\vartheta'(1)=0$ (adiabatic walls), the solution of (24b),

$$\vartheta=\Delta^5 \operatorname{Pr} \operatorname{Re}_s^2 (10x^3-3x^5-15x)/360, \tag{24d}$$

is similar to that obtained by Kirdyashkin.[7]

The third exception is the limiting case of $b\to 0$, where the term in (22) involving γ vanishes because both I and c are proportional to b. Then for the pipe flow case, (22) reduces to

$$(y\vartheta')'=-yw \operatorname{Pr} \operatorname{Re}_s^2/96. \tag{25}$$

Substituting w from (20a) and integrating (25) under conditions (23b) we get another compact polynomial solution,

$$\vartheta=(1-y^2)^3 \operatorname{Pr} \operatorname{Re}_s^2/1152. \tag{26}$$

Note that $\vartheta'(1)=0$ for (26), i.e., heat flux through the pipe wall is zero.

Figure 4(a) shows the radial profiles of temperature for different values of swirl b. Curve 0 represents the analytical solution (26) normalized by $\vartheta(0)$, while the other curves correspond to numerically determined solutions of the problem (22), (23b) at $\gamma=1.4$ and $\operatorname{Pr}=0.7$. We see that the temperature is higher near the axis than near the wall; this occurs because the near-axis flow originates at the hot end. For large swirl b (and therefore large axial velocity), the temperature near the wall drops below its value at the wall. This drop occurs because (i) the near-wall flow originates at the cold end and (ii) cooling by this high-speed flow overcompensates the radial heat conduction from the axis (we find that temperature even on the axis can drop below the wall temperature in a nonparallel flow; see Sec. VI).

F. Axial heat flux

Consider heat flux Q through a normal cross section ($z=\text{const}$),

$$Q=\int (\rho c_p v_z T-\kappa \partial T/\partial z) 2\pi r\, dr,$$

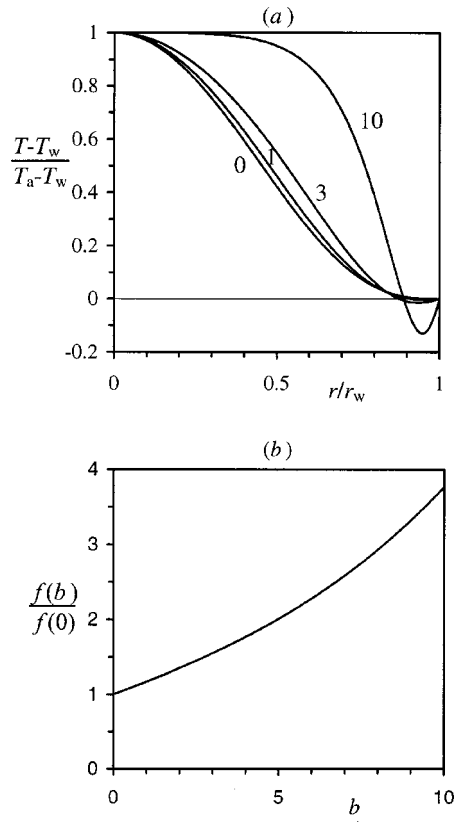

FIG. 4. (a) The dependence of the radial distribution of temperature on swirl b. Subscripts w and a indicate values at the wall and at the axis. (b) The dependence of heat flux $[\operatorname{Nu}=1+\operatorname{Ra}^2 f(b),\ f(0)=1/(120*96^2)]$ on swirl.

and introduce the Nusselt number, $\operatorname{Nu}=Q/Q_{\text{cond}}$, where $Q_{\text{cond}}=\int(-\kappa\partial T/\partial z)2\pi r\, dr$ is the heat flux due to conduction. Using the ϵ expansion and the dimensionless variables, and neglecting terms smaller than that of $O(\epsilon^2)$, we get

$$\operatorname{Nu}=1+2 \operatorname{Pr} \epsilon^2 \operatorname{Re}_s^2 b^{-1}(1-a^2)^{-1}\int_a^1 W\vartheta \exp Iy\, dy.$$

For a narrow annulus with adiabatic walls, this formula with the help of (18a) and (24c) reduces to

$$\operatorname{Nu}=1+2 \operatorname{Ra}^2/2835,$$

where $\operatorname{Ra}=\epsilon \operatorname{Pr} \operatorname{Re}_s^2 \Delta^4=\operatorname{Pr}|\partial T/\partial z|\rho_{0i}^2 g_c \delta^4/(T_0\mu^2)$.

According to experiment,[7] the above-mentioned solution is valid up to $\operatorname{Ra}=1500$ (Kirdyashkin[7] uses a different Rayleigh number, $\operatorname{Ra}_K=2\operatorname{Ra}^2/45$). At $\operatorname{Ra}=1500$, $\operatorname{Nu}\approx 1600$, i.e., the heat flux from the hot end to the cold end is larger by three orders of magnitude than that due to conduction. For $\operatorname{Ra}>1500$, the flow becomes slightly nonparallel and boundary layers develop near the walls as Ra further increases.

Kirdyashkin[7] found that there is no instability, at least up to $\operatorname{Ra}=15\,000$ at $\operatorname{Pr}=5-7$ (alcohol and water). In contrast, Gershuni, Zhukhovitskii, and Myznikov[8] found numerically that the flow becomes linearly unstable (to disturbances shaped as streamwise vortex rolls) at $\operatorname{Ra}=880$ for $\operatorname{Pr}>1$. This discrepancy may be due to the difference in the boundary conditions for temperature in these two studies: The experiment[7] was with adiabatic walls, i.e., for (24d), while the theory[8] dealt with fixed-temperature walls, i.e., for (24c).

For the pipe flow, we find that $\mathrm{Nu}=1+\mathrm{Ra}^2 f(b)$ where $\mathrm{Ra}=\epsilon\,\mathrm{Pr}\,\mathrm{Re}_s^2$ and $f(0)=1/(120*96^2)$, according to solutions (20a) and (26). Figure 4(b) shows the numerical results for $f(b)/f(0)$.

IV. END-WALL EFFECT

Solutions obtained in Sec. III describe flows away from the end walls of a cylindrical container (Fig. 1). Now we consider a simple model of the flow near the end walls. At the end walls, the axial velocity v_z must satisfy the no-slip condition and therefore v_z strongly depends on z near the end walls. As a flow turns around near an end wall, the radial velocity v_r becomes significant. In contrast to v_r and v_z, distributions of the azimuthal velocity v_ϕ, temperature, and density near an end wall are not necessarily very different from the distributions away. Therefore, in the following approximation we consider v_ϕ to be z independent and apply relations (4a), (8), and (10) to obtain solutions for v_r and v_z near the endwalls.

First, we introduce the Stokes stream function $\Psi(r,z)$:

$$v_z=(\rho r)^{-1}\partial\Psi/\partial r,\quad v_r=-(\rho r)^{-1}\partial\Psi/\partial z. \tag{27}$$

The continuity equation (1) is automatically satisfied by (27). Using (27) and excluding pressure from the r- and z-momentum equations in (1) we obtain up to $O(\epsilon)$,

$$\begin{aligned}&(\rho_0 r)^{-1}\partial^4\Psi/\partial z^4+\partial/\partial r[r^{-1}\partial/\partial r(\rho_0^{-1}\partial^2\Psi/\partial z^2)\\&\quad+(\rho_0 r)^{-1}\partial^3\Psi/\partial z^2\partial r]\\&\quad+\partial/\partial r[r^{-1}\partial/\partial r(r\partial/\partial r\{(\rho_0 r)^{-1}\partial\Psi/\partial r\})]\\&\quad=\epsilon(\mu r_0)^{-1}\rho_1 v_\phi^2/r.\end{aligned} \tag{28}$$

Next, we approximate Ψ as a product of a function of r and a function of z,

$$\Psi=\epsilon\rho_{0i}^2\mu^{-1}RT_R r_w^{-3}W(0)\Phi(z)Q(y),\quad \underline{z}=z/r_0,$$

where $Q(y)=\int_a^y y\exp(I)w(y)dy$, according to the first equation in (27) and (4b).

Then, integrating (28) in the radial direction from r_i to r_w we obtain

$$a_4\Phi''''-a_2\Phi''+a_0\Phi=a_r. \tag{29a}$$

Here the prime denotes differentiation with respect to $\underline{z}=z/r_w$. Values of constants a_4, a_2, a_0, and a_r follow from the solutions obtained in Sec. III. For example, for a pipe flow,

$$a_4=W(0)\int_0^1 y^{-1}\exp(-by^2/2)Q(y)dy,\quad a_2=2W(0),$$

$$a_0=(b/2-c)\exp(b/2)+c,\quad a_r=b^2/8+(1-c)b/2.$$

In the limiting case of $b\to 0$, we use (20a) to obtain $Q=y^2(1-y^2)^2/2$. Substituting $c=b/6$ and $W(0)=b/96$ we get $a_r=\frac{1}{2}b$, $a_0=\frac{1}{2}b$, and $a_2=b/48$, and by integrating we find $a_4=b/1152$. Then, (29a) becomes

$$\Phi''''-24\Phi''+576\Phi=576. \tag{29b}$$

Equation (29a) must be either integrated in the range, $-l\leqslant z\leqslant l$, where $2l$ is the length of a rotating cylindrical container (Fig. 1), under the no-slip conditions at $z=\pm l$, or (due to symmetry) in the range $0\leqslant z\leqslant l$ under the following conditions:

$$\begin{aligned}&\Phi'(0)=\Phi'''(0)=0\quad(\text{symmetry}),\\&\Phi(l)=\Phi'(l)=0\quad(\text{no-slip}).\end{aligned} \tag{30}$$

When the aspect ratio is large ($\underline{l}\equiv l/r_w\gg 1$), we expect that away from the end wall at $z=l$, Φ becomes z independent and that the particular solution of (29a), $\Phi_c=a_r/a_0$, is valid ($\Phi_c\to 1$ as swirl $b\to 0$). Near the end wall, Φ_c must be corrected with the help of solutions of the uniform version of (29a),

$$a_4\Phi''''-a_2\Phi''+a_0\Phi=0. \tag{31}$$

Solutions of (31) are exponential functions, $\exp(\lambda x)$, where λ are roots of the characteristic relation, $a_4\lambda^4-a_2\lambda^2+a_0=0$. Let $\lambda_1=\lambda_r+i\lambda_i$ be the root with $\lambda_r>0$ and $\lambda_i>0$ [e.g., $\lambda_1\approx 4.24+i2.45$ for (29b)]. The other three roots are symmetric in the other quadrants of the complex λ plane. The roots are independent of the aspect ratio l, and vary slightly with swirl b, as shown in Fig. 5.

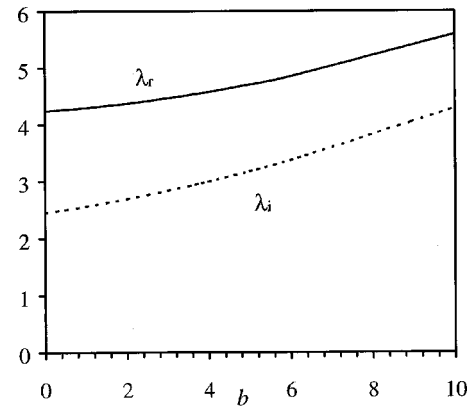

FIG. 5. Root $\lambda_r+i\lambda_i$ (characterizing the flow dependence on z) as a function on swirl b.

The solution of (29a), satisfying the no-slip conditions is

$$\begin{aligned}\Phi=\Phi_0\{&\lambda_1\sinh(\lambda_1\underline{l})[\cosh(\lambda_2\underline{l})-\cosh(\lambda_2\underline{z})]\\&-\lambda_2\sinh(\lambda_2\underline{l})[\cosh(\lambda_1\underline{l})-\cosh(\lambda_1\underline{z})]\},\end{aligned} \tag{32}$$

where $\Phi_0=a_r a_0^{-1}/\{\lambda_1\sinh(\lambda_1\underline{l})[\cosh(\lambda_2\underline{l})-1]-\lambda_2\sinh(\lambda_2\underline{l})\times[\cosh(\lambda_1\underline{l})-1]\}$, $\underline{l}=l/r_0$, and λ_2 is complex conjugate λ_1 (so Φ is real). Figure 6(a) shows $\Phi(z)$ at $b=1$.

Figures 6(b) and 6(c) depict stream surfaces in the meridional ($\phi=\text{const}$) cross section (only one quarter of the cross section is shown because of symmetry) at $b=0$ and $b=5$, respectively. The fluid flows from the cold end toward the hot end (say, from left to right) near the wall, $r=r_w$, and in the opposite direction near the axis, $r=0$. The axial extent of the region where the flow turns around near an end wall is close to r_w and does not depend on the cylinder length (for large l). As swirl increases, streamlines concentrate near the sidewall (compare the $b=0$ and $b=5$ flow patterns). We consider some other (more important and less obvious) effects of strong swirl in Secs. V and VI.

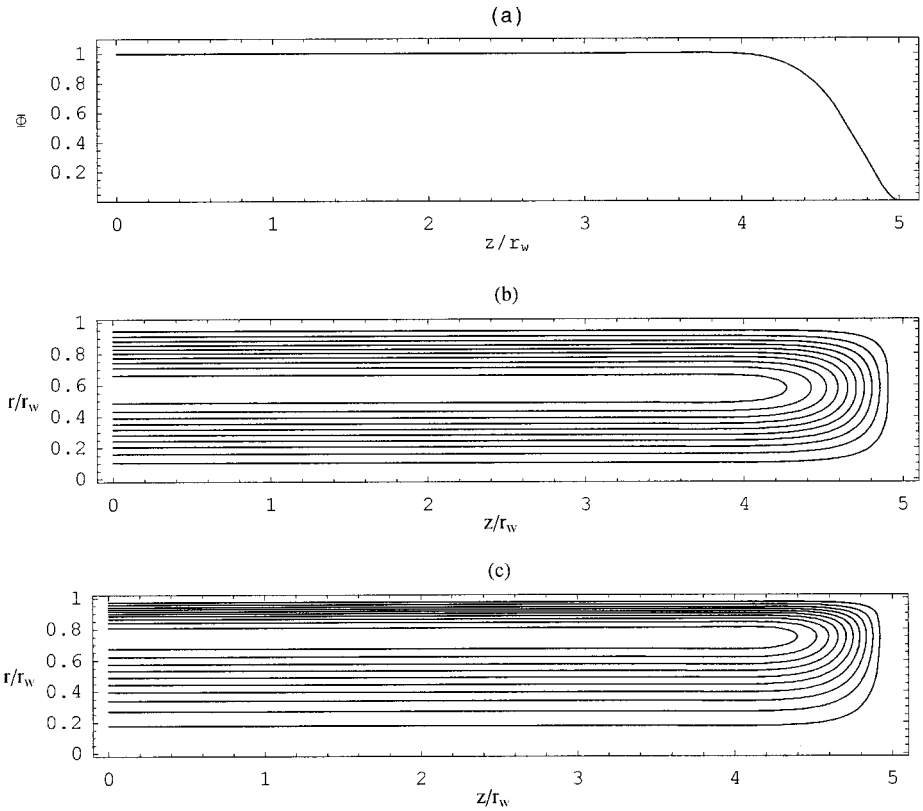

FIG. 6. (a) Dependence of the velocity at the axis on the axial coordinate. The velocity is normalized by its value in the center, $z=0$. (b), (c) Meridional cross section of stream surfaces at (b) weak ($b\to 0$) and (c) strong ($b=5$) swirl. All plots (a)–(c) are z symmetric.

V. MODERATE ROTATION

The flow studied in Secs. III and IV does not depend on the radial distribution of temperature (ϑ). This is due to the small-parameter expansion, where the swirl velocity is of $O(1)$, the axial velocity is of $O(\epsilon)$, and the radial temperature difference is of $O(\epsilon^2)$. Here, we consider the case of moderate rotation where the radial temperature difference, being of $O(1)$, strongly influences the flow, while the effect of v_r remains negligible.

According to solutions (24c), (24d), and (26), $\vartheta\sim \mathrm{Re}_s^2$ and $\epsilon^2\vartheta\sim\epsilon^2\,\mathrm{Re}_s^2$. Therefore, in the case of intense rotation, when $\mathrm{Re}_s\sim 1/\epsilon$, the term $\epsilon^2\vartheta$ in (21) is of $O(1)$. In such a case, ϑ must influence both the axial velocity and the density solutions. To account for this effect, we reconsider the small-parameter expansion for $\mathrm{Re}_s^*\equiv\epsilon\,\mathrm{Re}_s\sim O(1)$ in the current section and for $\mathrm{Re}_s^*\gg 1$ in Sec. VI.

First, we modify (5) to

$$T=T_R[\vartheta(r)-\epsilon z/r_w+O(\epsilon^2)], \tag{33}$$

while keeping (7) and (8) unchanged. Therefore, we must replace (4a) by

$$p_0(r)=RT_R\rho_0(r)\vartheta(r), \tag{34a}$$

and (9) by

$$p_1(r)=RT_R[\rho_0(r)-\vartheta(r)\rho_1(r)]. \tag{34b}$$

Thus, the radial variation of temperature (ϑ) now influences the pressure distribution via (34a) and (34b); this is a non-Boussinesq effect.

While the equation for swirl velocity is uncoupled (as we neglect v_r) and solution (3) remains valid, all other equations are now coupled. Here, we use ωr_w as the scale for both the swirl and axial velocities,

$$v_\phi=\omega r_w v(y),\quad v_z=\omega r_w w(y).$$

Also, we use ρ_R (reference density) as the scale for ρ_0 and ρ_1,

$$\rho_0(r)=\rho_R\rho_0^*(y),\quad \rho_1(r)=\rho_R\rho_1^*(y).$$

Then the coupled system for the dimensionless variables, ρ_0^*, ρ_1^*, w, and ϑ is

$$\rho_0^{*\prime}=\rho_0^* bv^2/y-\rho_0^*\vartheta'/\vartheta, \tag{35a}$$

$$\rho_1^{*\prime}=(\rho_1^*+\rho_0^*/\vartheta)(bv^2/y-\vartheta')/\vartheta, \tag{35b}$$

$$w''=b^{-1}\,\mathrm{Re}_s^*(\vartheta\rho_1^*-\rho_0^*)-w'/y, \tag{35c}$$

$$\vartheta''=\mathrm{Pr}\,\mathrm{Re}_s^* w[(1-\gamma)\vartheta\rho_1^*-\rho_0^*]/\gamma-\vartheta'/y, \tag{35d}$$

where the prime denotes differentiation with respect to $y=r/r_w$.

At the outer wall ($y=1$),

$$\rho_0^*(1)=1,\quad w(1)=0,\quad \vartheta(1)=1, \tag{36}$$

where $w(1)=0$ is the no-slip condition, while $\rho_0^*(1)=1$ and $\vartheta(1)=1$ indicate that the reference density and temperature are located at the outer wall. Now the swirl Reynolds number is also based on the density at the outer wall, $\mathrm{Re}_s=\rho_R\omega r_w/\mu$.

For a pipe flow, the symmetry conditions at the axis, $y=0$, are

$$w'(0)=0, \quad \vartheta'(0)=0. \tag{37a}$$

For an annular flow, the conditions at the inner wall, $y=a$, are

$$w(a)=0, \quad \vartheta(a)=1, \tag{37b}$$

where the condition $\vartheta(a)=1$ indicates that the temperature at the inner wall is the same as that at the outer wall. Finally, condition (15) (zero mass flow rate) must be satisfied with the help of an appropriate choice of a boundary value for ρ_1^*. This makes the problem mathematically closed.

In terms of the new variables, the dimensionless axial heat flux (Nu) is

$$\mathrm{Nu}=1+2\,\mathrm{Pr}\,\mathrm{Re}_s^*\epsilon^{-2}\int_a^1 \rho_0^* w\,\vartheta y\,dy. \tag{38}$$

Figure 7(a) shows the numerical results for the pipe flow at $\mathrm{Re}_s^*=20$. The swirl velocity v_ϕ, temperature T, and density ρ are normalized by their values at the wall, $r=r_w$. The axial velocity v_z is normalized by the wall azimuthal velocity ωr_w. In Fig. 7(a), we compare the results of the current section (solid curves), of Sec. III (the Boussinesq approximation, dashed curves), and of Sec. VI (dotted curves). Remarkably, the Boussinesq approximation overestimates T and underestimates ρ. While the dashed-line ρ curve shows centrifugal stratification of density at constant temperature [see the first term on the right-hand side of (35a)], the solid-line ρ curve shows also the additional effect of the radial gradient of temperature [the second term on the right-hand side of (35a)]. Thus, non-Boussinesq effects are clearly significant for large Re_s.

In the approximation used in the current section, the flow remains parallel. As Re_s^* further increases, nonparallel effects become significant and then boundary layers develop (as evidenced by the planar flow experiment[7]). To our knowledge, no theory has so far been developed to predict these effects. In Sec. VI we investigate weakly nonparallel effects and estimate an upper value of Re_s^* for which the expansion of Sec. V remains valid.

VI. RAPID ROTATION

One way to take into account nonparallel effects is to consider more terms in the small-parameter expansion. Here we include the $O(\epsilon)$ terms for velocity, which implies a modification of the $O(\epsilon)$ term for temperature. Therefore, we use (8) for density and the following new representations for velocity and temperature:

$$v_z=\omega r_w[w_0(y)+w_1(y)\epsilon z/r_w+O(\epsilon^2)], \tag{39a}$$

$$v_\phi=\omega r_w[v_0(y)+v_1(y)\epsilon z/r_w+O(\epsilon^2)], \tag{39b}$$

$$v_r=\epsilon\omega r_w[u_1(y)+O(\epsilon^2)], \tag{39c}$$

$$T=T_R[\vartheta_0(y)-\vartheta_1(y)\epsilon z/r_w+O(\epsilon^2)]. \tag{39d}$$

Thus, the $O(\epsilon)$ terms for all flow characteristics are now included. Higher-order terms (having indices other than 0 and 1) are neglected in this truncated representation. Note that the $O(\epsilon)$ term for dT/dz is r dependent according to (39d), in contrast to (5), (21), and (33).

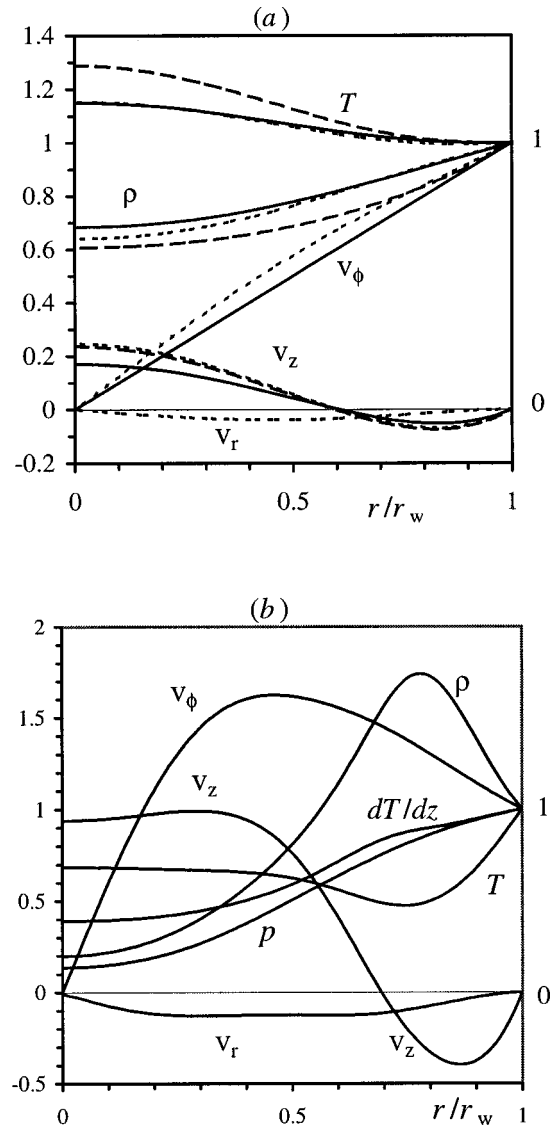

FIG. 7. The radial distribution of temperature T, density ρ (normalized by their values at the wall), swirl v_ϕ, and axial v_z velocities (normalized by ωr_w), and radial velocity v_r (normalized by $\epsilon\omega r_w$) at $\epsilon=0.01$, $b=0.5$, Pr $=0.7$, $\gamma=1.4$. (a) Boussinesq (dashed curves), parallel non-Boussinesq (solid curves), and weakly nonparallel (dotted curves) approximations at $\mathrm{Re}_s^*=20$, (b) nonparallel approximation at $\mathrm{Re}_s^*=60$, pressure p and axial gradient of temperature $dT\,dz$ are normalized by their wall values.

Substituting (8) and (39) in (1), we get the system for large $\mathrm{Re}_s^*\equiv\epsilon\,\mathrm{Re}_s$,

$$\rho_0'=\rho_0 b v_0^2/y-\rho_0\vartheta_0'/\vartheta_0,$$

$$v_0''=v_0/y^2-v_0'/y+\mathrm{Re}_s^*\,\rho_0(u_1v_0'+w_0v_1+u_1v_0/y),$$

$$w_0''=\mathrm{Re}_s^*\{\rho_0(u_1w_0'+w_0w_1)+b^{-1}(\rho_1\vartheta_0-\rho_0\vartheta_1)\}-w_0'/y,$$

$$\vartheta_0''=\mathrm{Pr}\,\mathrm{Re}_s^*\{\rho_0(u_1\vartheta_0'-w_0\vartheta_1)-(1-1/\gamma)[u_1b\rho_0v_0^2/y+w_0(\rho_1\vartheta_0-\rho_0\vartheta_1)]\}-\vartheta_0'/y,$$

$$\rho_1'=[\rho_0w_1+\rho_1w_0+(\rho_0'+\rho_0/y)u_1]/\vartheta_0,$$

$$u_1' = -yw_1 + u_1 + (y\rho_1 w_0 + \rho_0' y u_1)/\rho_0,$$

$$v_1'' = v_1/y^2 - v_1'/y + \mathrm{Re}_s^*[\rho_0(u_1 v_1' + w_1 v_1 + u_1 v_1/y) + \rho_1(u_1 v_0' + w_0 v_1 + u_1 v_0/y)],$$

$$w_1''' = \mathrm{Re}_s^*\{[\rho_1(u_1 w_0' + w_0 w_1) + \rho_0(u_1 w_1' + w_1 w_1)]' + 2(\rho_0 v_1^2 + 2\rho_1 v_0 v_1)/y\} - (w_1'/y)',$$

$$\vartheta_1'' = \mathrm{Pr}\,\mathrm{Re}_s^*\{\rho_1(u_1\vartheta_0' - w_0\vartheta_1) - \rho_0(u_1\vartheta_1' + w_1\vartheta_1) - (1-1/\gamma)[u_1 b(\rho_1 v_0^2 + 2\rho_0 v_0 v_1)/y + w_1(\rho_1\vartheta_0 - \rho_0\vartheta_1) - 2w_0\rho_1\vartheta_1]\} - \vartheta_1'/y.$$

The boundary conditions are no slip at the wall, symmetry on the axis, no total mass flux in the z direction, and the prescribed temperature at the wall: $\vartheta_0(1) = \vartheta_1(1) = 1$.

Figure 7(a) shows the numerical results for this nonparallel flow (dotted curves) at the same parameter values as those for the parallel flow [solid and dashed curves in Fig. 7(a) obtained in Secs. V and III, respectively]. The results of Secs. V and VI are close to each other for T and ρ, and the distribution of the azimuthal velocity v_ϕ only slightly differs from that for solid-body rotation. This difference is due to the radial velocity, which being negative (as the curve v_r depicts) transports angular momentum toward the axis. The radial velocity v_r (normalized by $\epsilon\omega r_0$ in Fig. 7) is very small at $\mathrm{Re}_s^* \equiv \epsilon\,\mathrm{Re}_s = 20$. Thus, by comparing the solid and dotted curves in Fig. 7(a), we conclude that the approach of Sec. V is valid for $\mathrm{Re}_s^* \leqslant 20$. For larger Re_s^*, the nonparallel nature of the flow causes significant new effects, as shown in Fig. 7(b) ($\mathrm{Re}_s^* = 60$).

The first important feature is that the radial velocity now radically redistributes the swirl. The v_ϕ maximum in Fig. 7(b) is no longer at the wall [unlike in Fig. 7(a)] and separates the vortex core (i.e., the region of nearly solid-body rotation) from the outer, nearly potential swirl. Such a v_ϕ profile is typical of vortex tubes.

The second important feature is that unlike in Fig. 7(a), density has its maximum (at constant z) away from the wall [curve ρ in Fig. 7(b)]. This occurs because (i) the temperature minimum is away from the wall (curve T) and (ii) temperature and density have strong dependence via (34a). It may be emphasized that unlike ρ and T, pressure ($\sim\rho T$) monotonically increases with r (curve p). The effect (i) is different from that shown in Fig. 4(a). At such small b ($=0.5$), there is no visible decrease in temperature below its wall value in Fig. 4(a), whereas temperature drops to *half* the wall value in Fig. 7(b). Such a remarkable decrease in temperature occurs due to the radial velocity, despite v_r being small. The radially inward convection (all along the pipe) opposes heat conduction away from the axis and thus enhances the temperature drop caused by the flow away from the cold end along the wall.

The third important feature is that temperature on the axis is smaller than at the wall in Fig. 7(b) [unlike in Fig. 7(a)]. Because pressure drops from the wall to the axis, adiabatic expansion cools the gas flowing inward. The pressure drop becomes so large for strong swirl (e.g., see curve p) that this cooling overcompensates heating from the hot end by the near-axis flow. While this heating increases temperature near the axis for small Re_s^* [Fig. 7(a), $\mathrm{Re}_s^* = 20$], adiabatic cooling due to the radial convergence of the flow decreases temperature for large Re_s^* [Fig. 7(b)], ($\mathrm{Re}_s^* = 60$).

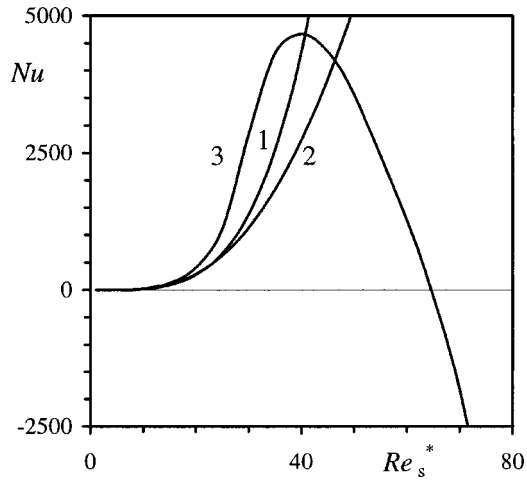

FIG. 8. The dependence of heat transfer (Nu) on swirl (Re_s^*) according to the parallel Boussinesq (curve 1), parallel non-Boussinesq (2) and nonparallel (3) approximations.

The fourth striking effect is that the total axial heat transfer (characterized by the Nusselt number Nu) decreases and even reverses (!) for intense swirl. Figure 8 shows $\mathrm{Nu}(\mathrm{Re}_s^*)$ for all the expansions used in this paper: curve 1, for the Boussinesq approximation (Sec. III); curve 2, for the parallel non-Boussinesq approximation (Sec. V); and curve 3, for the weakly nonparallel approach of the current section. While curves 1 and 2 depict the unbounded increase in heat transfer with swirl, curve 3 shows that Nu reaches its maximum and then decays (and even changes its sign). This decay results from the adiabatic cooling of the gas—an effect absent in the Boussinesq approximation, weak in the parallel non-Boussinesq approximation, and strong in the nonparallel flow for large Re_s^*. Our analysis thus reveals that for the maximizing heat transfer in centrifugal heat exchangers, swirl must neither be too small nor too large.

The fifth feature is that the axial gradient of temperature, dT/dz, decreases with r [Fig. 7(b)]. Therefore, in contrast to the weak-swirl case, where dT/dz is uniform, for strong swirl dT/dz significantly diminishes near the axis compared to its prescribed value at the wall. While no data exists for cylindrical flows, such nearly uniform temperature away from the walls has indeed been observed in the planar flow[7] (this difference in geometry is not central to the effect).

These nonparallel effects appear even though the radial velocity v_r [which in Fig. 7(b) is three times that in Fig. 7(a)] remains small compared with v_ϕ and v_z [Fig. 7(b)]. Thus, the nonparallel character of the flow becomes important for large $\mathrm{Re}_s^*(>20)$. Although our nonparallel approximation clearly reveals this fact, this approximation has its limitations, in particular, concerning the z extent of the flow, as Fig. 9 illustrates.

Pursuing the nonparallel character of the meridional flow, Fig. 9 depicts streamlines at different swirl Reynolds

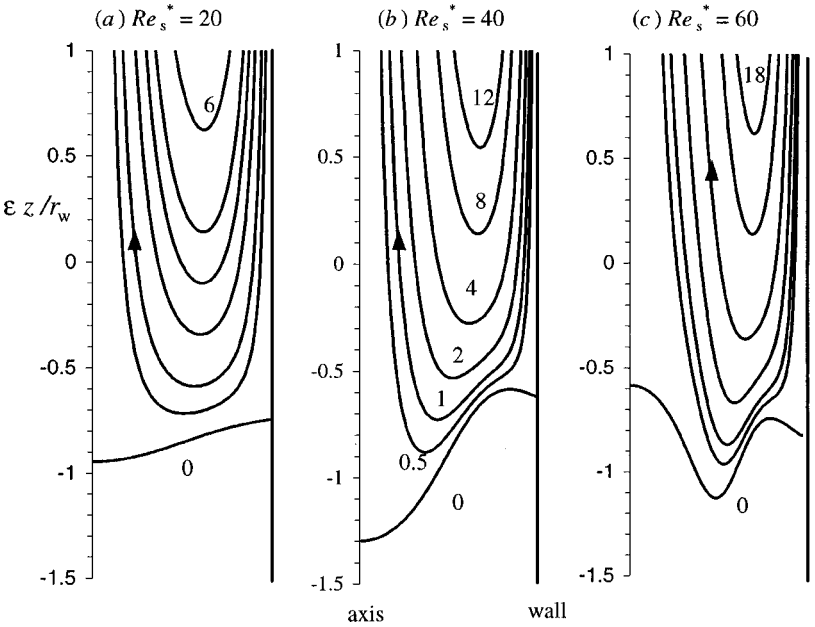

FIG. 9. Streamlines of the nonparallel flow at different swirl; (b) corresponds to the maximum heat transfer (see curve 3 in Fig. 8).

numbers: (a) $\mathrm{Re}_s^*=20$ [same as in Fig. 7(a)], (b) $\mathrm{Re}_s^*=40$, where Nu is maximum (curve 3 in Fig. 8), and (c) $\mathrm{Re}_s^*=60$ [same as in Fig. 7(b)]. An artifact of the truncation in the z expansion is that the flow terminates at curves 0 in Fig. 9 (where curve labels indicate values of the scaled stream function Ψ). Recall that the truncation yields negative temperature for $\epsilon z/r_w>1$ [e.g., see (5)]. Therefore, the approach is certainly invalid for large $|\epsilon z/r_w|$, say for $|\epsilon z/r_w|>0.5$.

As swirl intensifies, streamlines in Fig. 9 concentrate near the wall (as in Fig. 6) and become skewed (unlike in Fig. 6). The skewed flow pattern in Fig. 9(b) qualitatively agrees with that experimentally observed near the hot end of the planar flow,[7] which becomes asymmetric with respect to the midplane. The shift of streamlines away from the axis in Fig. 9(c) is consistent with the v_z profile in Fig. 7(b), where the v_z maximum is located away from the axis [unlike in Fig. 7(a)], i.e., the near-axis flow becomes annular. The annular flow may serve as a precursor for possible flow reversal near the axis as swirl further increases. To find this and other nonparallel effects, a two-dimensional flow should be considered, since the truncation in our nonparallel approach becomes invalid for very large Re_s^*.

The nonparallel effects revealed in the current section are qualitatively different from those in Sec. IV. There, the flow becomes nonparallel only near the end walls, and the flow pattern is z symmetric (Fig. 6). Here, the flow pattern is *not* z symmetric (Fig. 9) and the flow is nonparallel even far away from end walls (note that the pipe is unbounded and that v_r is the same at all z!). The streamlines turn around here not because of the end walls (as in Sec. IV) but because of the axial gradient of temperature and the equation of state (2f) (i.e., non-Boussinesq effects) that together induce the radial velocity. In the Boussinesq approximation, the flow in the unbounded pipe remains parallel (Sec. III) as in the planar case.[6] In contrast, the results of the current section show that the streamlines converge to the axis not only near the hot end wall but also away from both end walls; that is, the convergence occurs in the bulk of the flow while the divergence occurs only near the cold end.

We assume that a similar flow pattern occurs in Ranque tubes and results in energy separation. Figure 10 shows our interpretation of the meridional flow in a Ranque tube. The incoming gas goes to the hot exit in annular region I and to the cold exit in the U-shaped region II. In circulatory domain III, the flow converges toward the axis, except near the cold end. The dashed lines show stream surfaces separating these regions. The bulk flow convergence and the pressure drop toward the axis (due to the centrifugal effect) cause adiabatic cooling. Furthermore, the gas entering the vortex core [say, $r/r_w<0.4$, as for curve v_ϕ in Fig. 7(a)] loses its kinetic energy due to (turbulent) diffusion occurring away from the axis. Therefore, stagnation temperature decreases near the axis and increases near the wall. This energy separation and

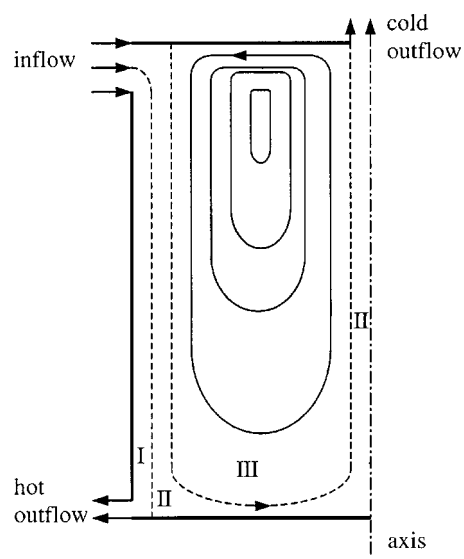

FIG. 10. Schematic of the meridional flow in a Ranque tube (not in scale).

the counterflow induce an axial gradient of temperature even without external heating and cooling (in contrast to heat exchangers). Therefore, centrifugal convection is self-sustained in a Ranque tube. This centrifugal convection drives the meridional circulation in domain III (occupying a large part of the flow region). Note that the meridional circulation persists even when the hot outlet is closed (region I shrinks) or the cold outlet is closed (region II shrinks).

While it seems reasonable that centrifugal convection drives the counterflow in Ranque tubes, the situation in hydrocyclones appears more enigmatic. Why does the near-axis backflow occur along the whole axial extent of hydrocyclones despite turbulent mixing? The only explanation is that a favorable axial gradient of pressure develops along the axis. Such a pressure distribution can also result from centrifugal convection.

Although the temperature difference in hydrocyclones (e.g., due to thermal dissipation) is significantly smaller than in Ranque tubes, the radial gradient of pressure in hydrocyclones is large due to a huge liquid to gas density ratio. A small axial gradient of temperature and a large radial gradient of pressure can cause an axial gradient of pressure along the axis, which is opposite to that along the wall (as shown in Fig. 1). This axial gradient of pressure drives a backflow near the axis. If our inference is true, centrifugal convection should be a generic phenomenon in vortex devices.

An open question is flow stability. The fact that density stratification near the wall becomes unstable [curves ρ in Fig. 7(b)] can cause the appearance of convection cells. Fortunately, the unstable layer is located inside the unidirectional near-wall flow, while near the inflexion point of the axial velocity profile, density stratification is stable and the density gradient is large [compare curves ρ and v_z in Fig. 7(b)]. Therefore, the convection-driven counterflow studied in this paper seems to be stable and provides efficient heat exchange in the axial direction. These features require verification by stability studies.

VII. CONCLUDING REMARKS

Motivated by the search for the driving mechanism for a centrifugal heat exchanger, we have obtained analytical and numerical solutions describing flows of a compressible fluid induced by the axial gradient of temperature in a rotating pipe and in a cylindrical annulus. Contrary to the case where acceleration and heat flux are parallel, no equilibrium state exists in the problem considered here, in which acceleration and heat flux are orthogonal: even an arbitrarily small temperature gradient induces centrifugal convection—flow from the cold end to the hot end along the wall and backflow near the axis.

Such counterflows survive intense turbulent mixing for high Reynolds numbers in vortex tubes and hydrocyclones (even when their length to diameter ratio exceeds 100). This survival results from the pressure gradient driving the backflow along all the axial extent of these devices. Our analytical solutions explicitly show that the axial gradient of pressure, $\partial p/\partial z$, has opposite directions near the wall and near the axis that explains the counterflow. For example, for weak

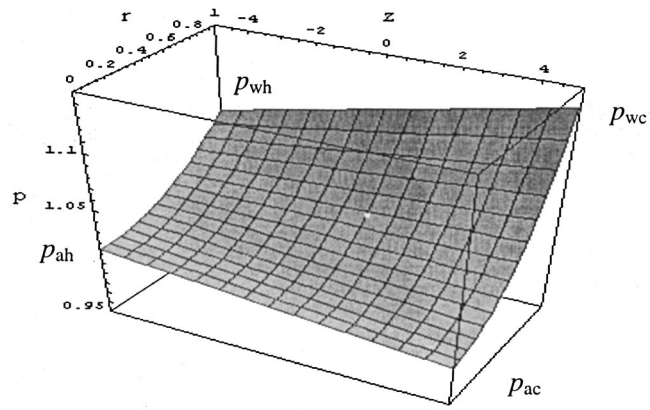

FIG. 11. Pressure distribution in the meridional cross section of a rotating pipe with the axial gradient of temperature.

rotation, $\partial p/\partial z \sim 3y^2-1$, i.e., $\partial p/\partial z>0$ at the wall ($y=1$) and $\partial p/\partial z<0$ on the axis ($y=0$). Figure 11 shows the pressure field on a half of the meridional cross section of the pipe, $0\leqslant r\leqslant r_w$ and $-l\leqslant z\leqslant l$. In Fig. 11, both r and z are normalized by r_w; p is normalized by p_R; $l=5r_w$, $T_h=700\,\mathrm{K}$, $T_c=300\,\mathrm{K}$, and $b=0.2$.

Pressure distribution provided by centrifugal convection (as shown in Fig. 11) makes the counterflow axially elongated. In contrast, vortex breakdown above delta wings and in sealed containers has a short counterflow.

Furthermore, our results indicate a possibility of vortex breakdown suppression with the help of centrifugal convection: For example, in a sealed cylinder with one rotating end wall, cooling this end wall and heating the fixed end wall should eliminate vortex-breakdown ''bubbles.''

Our results reveal an interesting non-Boussinesq effect: the bulk-flow convergence toward the axis when swirl is rapid. This convergence induced by a strong radial gradient of pressure (Fig. 11) causes the radial distribution of temperature that seems, at the first sight, paradoxical: Despite the fact that the flow moves from the hot end near the axis, temperature on the axis becomes lower than the wall temperature [curve T in Fig. 7(b)].

This practically important effect occurs due to radial velocity (even being very weak). First, radial convection, being directed toward the axis, opposes radial thermal conduction. This makes the temperature minimum near the wall (induced by the flow from the cold end) remarkably smaller than the wall temperature. Second, the radial flow transports this cold gas toward the axis. Since pressure drops from the wall to the axis, the gas is cooled further by adiabatic expansion. This cooling overcomes heating (due to the flow from the hot end near the axis) when rotation is rapid.

As a result, the flow near the axis transports the cooled gas to the cold end (!) while angular momentum and kinetic energy diffuse from the axis; this leads to energy separation (the Ranque effect). Due to this effect, the axial heat flux (characterized by the Nusselt number Nu) reaches its maximum and then decreases, as swirl further intensifies (curve 3 in Fig. 8).

Our estimates, based on the solutions obtained here, show that Nu becomes large ($>10^3$) for moderate values of

the Rayleigh number, $\mathrm{Ra}=(\epsilon\,\mathrm{Pr}\,\mathrm{Re}_s^2)\sim 10^3$. An open question is whether the meridional flow is stable for these Ra values. Experimental results[7] show that the horizontal flow remains laminar for such Ra. In the rotating cylindrical flows, there are two significant factors (absent in the horizontal case), which should stabilize the counterflow: (i) the Taylor–Proudman constraint and (ii) strong density stratification in the radial direction due to the centrifugal effect. So we expect that the flow is stable for even larger Ra than in the planar case. Nevertheless, the stability problem requires further studies.

ACKNOWLEDGMENTS

This research was partially supported by NSF Grant No. CTS 9904328.

[1] V. Barcilon and J. Pedlosky, ''On the steady motions produced by a stable stratification in a rapidly rotating fluid,'' J. Fluid Mech. **29**, 673 (1967).
[2] G. M. Homsy and J. L. Hudson, ''Centrifugal convection and its effect on the asymptotic stability of a bounded rotating fluid heated from below,'' J. Fluid Mech. **48**, 605 (1971).
[3] J. E. Hart, ''On the influence of centrifugal buoyancy on rotating convection,'' J. Fluid Mech. **403**, 133 (2000).
[4] F. H. Busse, ''Thermal instabilities in rapidly rotating systems,'' J. Fluid Mech. **44**, 441 (1970).
[5] J. Herrmann and F. H. Busse, ''Convection in a rotating cylindrical annulus. Part 4. Modulation and transition to chaos at low Prandtl numbers,'' J. Fluid Mech. **350**, 209 (1997).
[6] R. V. Birikh, ''Thermocapillary convection in a horizontal layer of liquid,'' J. Appl. Mech. Tech. Phys. **7**, 43 (1966).
[7] A. G. Kyrdyashkin, ''Thermogravitational and thermocapillary flows in a horizontal liquid layer under the conditions of a horizontal temperature gradient,'' Int. J. Heat Mass Transf. **27**, 1205 (1984).
[8] G. Z. Gershuni, E. M. Zhukhovitskii, and V. M. Myznikov, ''Stability of plane-parallel convective flow in a horizontal layer relative to spatial perturbations,'' J. Appl. Mech. Tech. Phys. **15**, 706 (1975).